Article

Kinetic and Mechanistic Investigations of Hydrothermal Transformations in Zinc Phosphates

Alexander J. Norquist, and Dermot O'Hare

J. Am. Chem. Soc., **2004**, 126 (21), 6673-6679• DOI: 10.1021/ja049860w • Publication Date (Web): 08 May 2004

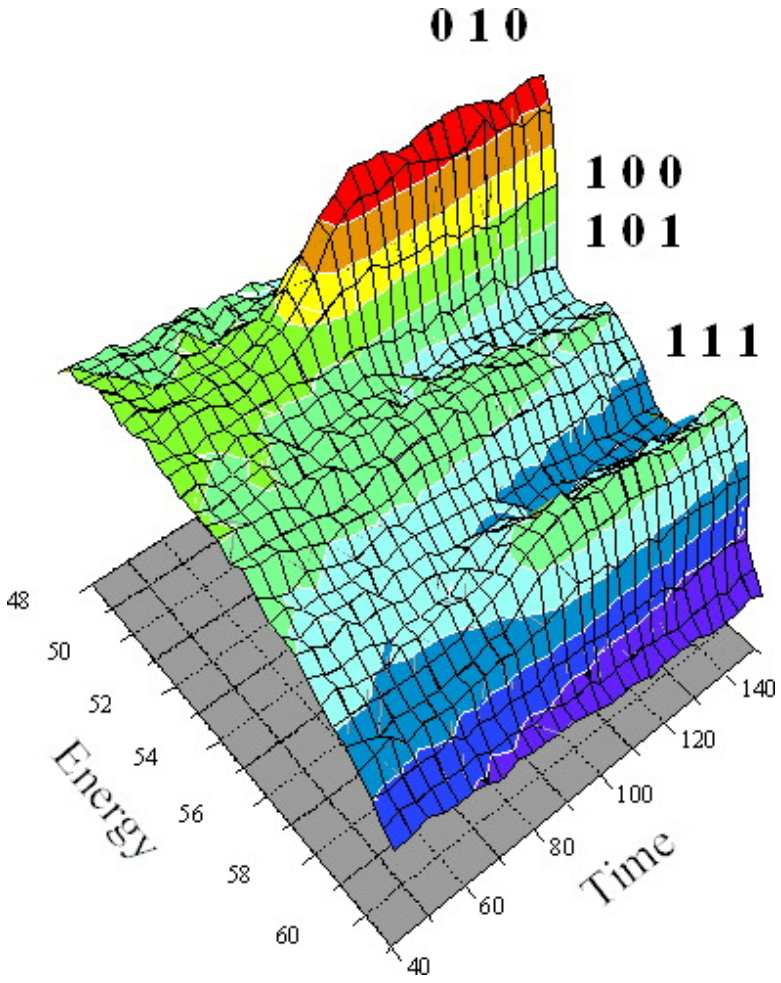

More About This Article

Additional resources and features associated with this article are available within the HTML version:

J|A|C|S
ARTICLES
Published on Web 05/08/2004

Kinetic and Mechanistic Investigations of Hydrothermal Transformations in Zinc Phosphates

Alexander J. Norquist[†] and Dermot O'Hare*[,‡]

Contribution from the Department of Chemistry, Haverford College, Haverford, Pennsylvania 19041, and Inorganic Chemistry Laboratory, University of Oxford, Oxford OX1 3QR, United Kingdom

Received January 9, 2004; E-mail: dermot.ohare@chem.ox.ac.uk

Abstract: The room-temperature crystallization of $[C_6N_2H_{18}][Zn(HPO_4)(H_2PO_4)_2]$, an organically templated zinc phosphate containing $[Zn_2(HPO_4)_2(H_2PO_4)_4]^{4-}$ molecular anions, and its transformation to compounds containing either one- or two-dimensional inorganic components, $[C_6N_2H_{18}][Zn_3(H_2O)_4(HPO_4)_4]$, $[C_4N_2H_{12}][Zn(HPO_4)_2(H_2O)]$, or $[C_3N_2H_6][Zn_4(OH)(PO_4)_3]$, under hydrothermal conditions were studied in-situ using energy-dispersive X-ray diffraction. The ability to collect data during reactions in a large volume (~23 mL) Teflon-lined autoclave under real laboratory conditions has allowed for the elucidation of kinetic and mechanistic information. Kinetic data have been determined by monitoring changes in the integrated peak intensities of Bragg reflections and have been modeled using the Avrami−Erofe'ev expression. The crystallization of $[C_6N_2H_{18}][Zn(HPO_4)(H_2PO_4)_2]$ is a diffusion-controlled process, while nucleation is increasingly more important in determining the overall rate of the formation of $[C_6N_2H_{18}][Zn_3(H_2O)_4(HPO_4)_4]$, $[C_4N_2H_{12}][Zn(HPO_4)_2(H_2O)]$, and $[C_3N_2H_6][Zn_4(OH)(PO_4)_3]$. The transformation of $[C_6N_2H_{18}][Zn(HPO_4)(H_2PO_4)_2]$ to $[C_4N_2H_{12}][Zn(HPO_4)_2(H_2O)]$ and $[C_3N_2H_6][Zn_4(OH)(PO_4)_3]$ occurs via a dissolution−reprecipitation mechanism, while the transformation to $[C_6N_2H_{18}][Zn_3(H_2O)_4(HPO_4)_4]$ may be the first observation of a direct topochemical conversion of one organically templated solid to another under hydrothermal conditions.

Introduction

Open-framework metal phosphates have been the focus of intense research since the discovery of zeolite-like aluminum phosphates in the early 1980s[1,2] because of their potential application in areas such as shape-selective catalysis, molecular sieving, and gas absorption.[3,4] A dramatic increase in structural diversity accompanied the incorporation of new transition and main group metals, because of their ability to have coordination numbers greater than 4, a limitation of aluminosilicate zeolites. Open-framework metal phosphates have been found to readily accept the inclusion of various metals.

Sustained interest in these compounds exists because the facile formation of novel structure types and potential for tunable properties outweighs the lack of thermal stability when compared to the aluminosilicate zeolites. For example, SAPO-11 is used as a support for a platinum lube-dewaxing catalyst on an industrial scale,[5] and transition metal-substituted aluminophosphates can catalyze the oxidation of alkanes.[6]

Despite the abundance of reported compounds and promise of desirable physical properties, several factors contribute to the lack of control in these reactions. First, the use of hydrothermal conditions during synthesis requires that robust pressure vessels be employed, which make direct observation during reaction difficult. Second, the high number of reaction variables present, including temperature, reaction time, solvent and reactant concentrations, and percent fill, contributes to a complex, interrelated reaction dynamic. A number of possible reaction mechanisms have been postulated for the formation of several families of microporous solids,[7−10] including those predicted using computer modeling.[11−13] Until recent years, little experimental data were available to enable a greater understanding of the complex processes involved in the formation of microporous materials.

The in-situ study of hydrothermal reactions using a noninvasive probe to follow reaction dynamics has begun to provide the first information toward the formulation of reaction mechanisms.[14,15] X-ray diffraction has proven to be a useful technique as it allows for the formation of crystalline phases to be monitored quantitatively. This technique has been used to study

[†] Haverford College.
[‡] University of Oxford.

(1) Wilson, S. T.; Lok, B. M.; Messina, C. A.; Cannan, T. R.; Flanigen, E. M. *J. Am. Chem. Soc.* **1982**, *104*, 1146.
(2) Wilson, S. T.; Lok, B. M.; Messina, C. A.; Cannon, T. R.; Flanigen, E. M. *ACS Symp. Ser.* **1983**, *218*, 79.
(3) Haag, W. O. *Zeolites Relat. Microporous Mater.* **1994**, *84B*, 1375.
(4) Zones, S. I.; Davis, M. E. *Curr. Opin. Solid State Mater. Chem.* **1996**, *1*, 107.
(5) Miller, S. *Microporous Mater.* **1994**, *2*, 439.
(6) Thomas, J. M.; Raja, R.; Sankar, G.; Bell, R. *Nature* **1999**, *398*, 226.
(7) Férey, G. *J. Fluorine Chem.* **1995**, *72*, 187.
(8) Oliver, S.; Kuperman, A.; Ozin, G. A. *Angew. Chem., Int. Ed.* **1998**, *37*, 46.
(9) Férey, G. *Chem. Mater.* **2001**, *13*, 3084.
(10) Rao, C. N. R.; Natarajan, S.; Choudhury, A.; Neeraj, S.; Ayi, A. A. *Acc. Chem. Res.* **2001**, *34*, 80.
(11) Lewis, D. W.; Catlow, C. R. A.; Thomas, J. M. *Faraday Discuss.* **1997**, *106*, 451.
(12) Lewis, D. W.; Sankar, G.; Wyles, J. K.; Thomas, J. M.; Catlow, C. R. A.; Willcock, D. J. *Angew. Chem., Int. Ed. Engl.* **1997**, *36*, 2675.
(13) Sefcik, J.; Goddard, W. A. *Geochim. Cosmochim. Acta* **2001**, *65*, 4435.
(14) Cheetham, A. K.; Mellot, C. F. *Chem. Mater.* **1997**, *8*, 2269.
(15) Francis, R. J.; O'Hare, D. *J. Chem. Soc., Dalton Trans.* **1998**, 3133.

10.1021/ja049860w CCC: $27.50

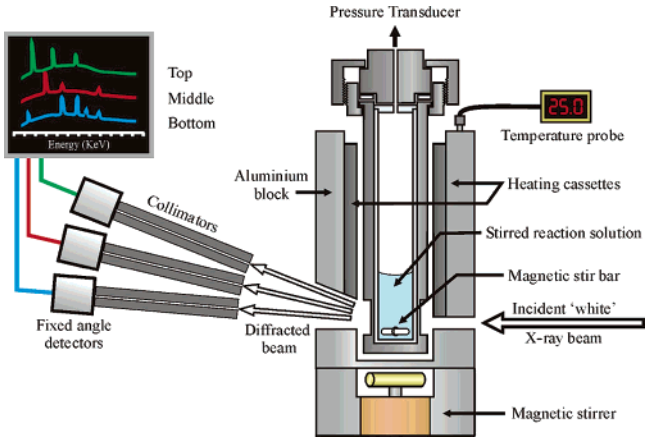

Figure 1. A schematic of the experimental apparatus used on Station 16.4 of the SRS at the Daresbury Laboratory.

the formation of transition metal aluminum phosphates, using angular[16−19] and energy-dispersive X-ray diffraction.[20−22] The ability to use laboratory size reaction vessels is an advantage that energy-dispersive X-ray diffraction (EDXRD) holds over angular-dispersive X-ray diffraction (ADXRD). The use of small, thin-walled vessels and a monochromatic X-ray source is generally required for in-situ ADXRD, while workers at Oxford and the U.K. Synchrotron Radiation Source have reported an EDXRD technique that uses only slightly modified reaction vessels.[23−25] A schematic of the EDXRD hydrothermal apparatus is shown in Figure 1.

We have used this experimental apparatus to study two families of microporous materials, gallium phosphates and zinc phosphates. The investigation of organically templated gallium phosphates has resulted in the first observation of a transient crystalline intermediate in a hydrothermal reaction[26,27] and the elucidation of both kinetic and mechanistic information for the synthesis of several compounds.[28−30] The work on zinc phosphates has been focused upon syntheses using amine phosphate starting materials.[31,32] The work presented in this report is focused upon the transformation of low dimensional zinc phosphates to those of higher dimensionality.[33,34] $[C_6N_2H_{18}][Zn(HPO_4)(H_2PO_4)_2]$ (denoted ZPM-I, the zinc phosphate monomer)[35] contains molecular $[Zn_2(HPO_4)_2(H_2PO_4)_4]^{4-}$ anions that have been shown to transform to inorganic frameworks that exhibit either one-, two-, or three-dimensionality.[33,35] A kinetic and mechanistic analysis of the crystallization of ZPM-I, and its transformation to $[C_6N_2H_{18}][Zn_3(H_2O)_4(HPO_4)_4]$ (ZnPO-TMED-I),[35] $[C_4N_2H_{12}][Zn(HPO_4)_2(H_2O)]$ (ZnPO-PIP-I),[36] and $[C_3N_2H_6][Zn_4(OH)(PO_4)_3]$ (ZnPO-IMID-I),[37] is reported in this paper. The inorganic components of these compounds are shown in Figure 2.

Experimental Section

Materials. ZnO (Aldrich, 99%), $ZnSO_4 \cdot 7H_2O$ (Aldrich, 99%), HCl (Fisher, 32% in water), piperazine (Aldrich, 99%), imidazole (Aldrich, 99%), and *N*,*N*,*N*′,*N*′-tetramethylethylenediamine (tmed, Aldrich, 99.5%) were used as received. Deionized water was used in these syntheses. $[C_6N_2H_{18}][HPO_4] \cdot 2H_2O$ (TMED-P)[38] was prepared using a previously reported method.[32]

In-Situ EDXRD. Energy-dispersive X-ray diffraction experiments were performed on Station 16.4 of the U.K. SRS at the Daresbury Laboratory using apparatus previously described.[23] The synchrotron source operates with an average stored current of 200 mA and a typical beam energy of 2 GeV. Station 16.4 is illuminated with radiation from a 6 T superconducting wiggler and receives X-rays over an energy range 5−120 keV with a maximum X-ray flux of 3×10^{10} photons s^{-1} at around 13 keV. The position of this energy maximum is shifted by the absorption of lower energy photons by the apparatus so that in practice X-rays with energies above ∼30 keV are useful. The hydrothermal cell has a volume similar to those available commercially for laboratory use (23 mL), but has a thinned stainless steel outer case (0.4 mm) to minimize absorption of X-rays. A series of experiments was performed, including the synthesis of ZPM-I and its transformation to ZnPO-TMED-I, ZnPO-PIP-I, and ZnPO-IMID-I under hydrothermal conditions. Gel compositions are listed in Table 1. In each reaction, ∼1−2 g of metal source was dispersed in ∼10 mL of deionized water by stirring with use of a magnetic stir bar. The amine was added, and the mixture was stirred for a few moments and then sealed in the cell and transferred to the preheated apparatus. The time between mixing reagent and the beginning of the data collection was always less than 5 min. Approximately 2−3 min elapsed between placing the autoclave into the heating block and opening the shutter for data collection. The introduction of the cold cell into the heated block caused cooling of the heating block, although the desired temperature was reached within ∼5 min. The reaction mixture was stirred continually during data collection to ensure solid material remained in the beam at all times and did not settle out. X-ray diffraction patterns were recorded every 60 s by a three-element solid-state detector, described by Colston et al.[39] Each detector element is separated by an angle of ∼3° in 2θ so that a *d*-spacing range of greater than 20 Å may be observed in a given experiment. In the current work, the lower detector was always set at $2\theta \approx 2.0°$, so that strong high *d*-spacing Bragg reflections appear in the region of the optimum energy position of the energy-dispersive

(16) Norby, P.; Christensen, A. N.; Hanson, J. C. *Stud. Surf. Sci. Catal.* **1994**, *84*, 179.
(17) Christensen, A. N.; Norby, P.; Hanson, J. C. *Acta Chem. Scand.* **1997**, *51*, 249.
(18) Christensen, A. N.; Jensen, T. R.; Norby, P.; Hanson, J. C. *Chem. Mater.* **1998**, *10*, 1688.
(19) Norby, P.; Hanson, J. C.; Fitch, A. N.; Vaughan, G.; Flaks, L.; Gualtieri, A. *Chem. Mater.* **2000**, *12*, 1473.
(20) Rey, F.; Sankar, G.; Thomas, J. M.; Barrett, P. A.; Lewis, D. W.; Catlow, C. R. A.; Clark, S. M.; Greaves, G. N. *Chem. Mater.* **1995**, *7*, 1435.
(21) Rey, F.; Sankar, G.; Thomas, J. M.; Barrett, P. A.; Lewis, D. W.; Catlow, C. R. A.; Clark, S. M.; Greaves, G. N. *Chem. Mater.* **1996**, *8*, 590.
(22) Davies, A. T.; Sankar, G.; Catlow, C. R. A.; Clark, S. M. *J. Phys. Chem. B* **1997**, *101*, 10115.
(23) Evans, J. S. O.; Francis, R. J.; O'Hare, D.; Price, S. J.; Clarke, S. M.; Flaherty, J.; Gordon, J.; Nield, A.; Tang, C. C. *Rev. Sci. Instrum.* **1995**, *66*, 2442.
(24) Clark, S. M.; Nield, A.; Rathbone, T.; Flaherty, J.; Tang, C. C.; Evans, J. S. O.; Francis, R. J.; O'Hare, D. *Nucl. Instrum. Methods B* **1995**, *97*, 98.
(25) Francis, R. J.; Price, S. J.; Evans, J. S. O.; O'Brien, S.; O'Hare, D.; Clark, S. M. *Chem. Mater.* **1996**, *8*, 2102.
(26) Francis, R. J.; Price, S. J.; O'Brien, S.; Fogg, A. M.; O'Hare, D.; Loiseau, T.; Férey, G. *Chem. Commun.* **1997**, 521.
(27) Francis, R. J.; O'Brien, S.; Fogg, A. M.; Halasyamani, P. S.; O'Hare, D.; Loiseau, T.; Férey, G. *J. Am. Chem. Soc.* **1999**, *121*, 1002.
(28) Walton, R. I.; Loiseau, T.; O'Hare, D.; Férey, G. *Chem. Mater.* **1999**, *11*, 1, 3201.
(29) Walton, R. I.; Millange, F.; O'Hare, D.; Paulet, L.; Loiseau, T.; Férey, G. *Chem. Mater.* **2000**, *12*, 1977.
(30) Millange, F.; Walton, R. I.; Guillou, N.; Loiseau, T.; O'Hare, D.; Férey, G. *Chem. Mater.* **2002**, *14*, 4448.
(31) Walton, R. I.; Norquist, A. J.; Neeraj, S.; Natarajan, S.; Rao, C. N. R.; O'Hare, D. *Chem. Commun.* **2001**, 1990.
(32) Walton, R. I.; Norquist, A. J.; Smith, R. I.; O'Hare, D. *Faraday Discuss.* **2002**, *122*, 331.
(33) Ayi, A. A.; Choudhury, A.; Natarajan, S.; Rao, C. N. R. *J. Mater. Chem.* **2000**, *10*, 2606.
(34) Choudhury, A.; Neeraj, S.; Natarajan, S.; Rao, C. N. R. *J. Mater. Chem.* **2001**, *11*, 1537.
(35) Neeraj, S.; Natarajan, S.; Rao, C. N. R. *J. Solid State Chem.* **2000**, *150*, 417.
(36) Rao, C. N. R.; Natarajan, S.; Neeraj, S. *J. Am. Chem. Soc.* **2000**, *122*, 2810.
(37) Natarajan, S.; Neeraj, S.; Rao, C. N. R. *Solid State Sci.* **2000**, *2*, 87.
(38) Neeraj, S.; Natarajan, S.; Rao, C. N. R. *Angew. Chem., Int. Ed.* **1999**, *38*, 3480.
(39) Colston, S. L.; Jacques, S. D. M.; Barnes, P.; Jupe, A. C.; Hall, C. *J. Synchrotron Radiat.* **1998**, *5*, 112.

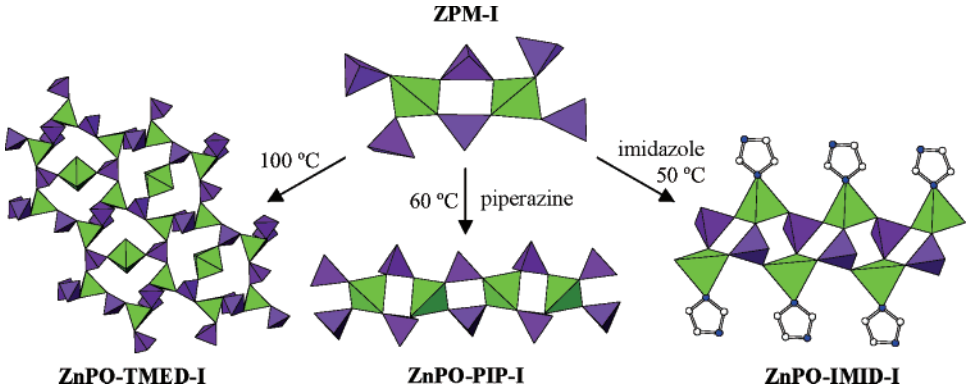

Figure 2. Representations of the inorganic frameworks present in ZPM-I, ZnPO-TMED-I, ZnPO-PIP-I, and ZnPO-IMID-I. Green and purple polyhedra contain Zn^{2+} and P^{5+} centers, respectively.

Table 1. Gel Compositions and Temperatures Used To Prepare ZPM-I, ZnPO-TMED-I, ZnPO-PIP-I, and ZnPO-IMID-I

compound	temp (°C)	amine	gel composition
ZPM-I	25	tmed	$ZnSO_4 \cdot 7H_2O$:$40H_2O$:$[C_6N_2H_{18}][HPO_4] \cdot 2H_2O$
ZnPO-TMED-I	100	tmed	ZPM-I:$100H_2O$
ZnPO-PIP-I	60	piperazine	ZPM-I:piperazine:$250H_2O$
ZnPO-IMID-I	50	imidazole	ZPM-I:2 imidazole:$350H_2O$

spectrum. For the energy-dispersive diffraction experiment, E (keV) $= 6.19926/(d \sin \theta)$ for a Bragg reflection arising from a plane of d (in angstroms).

Ex-Situ Characterization. All reaction products were characterized using both in-situ EDXRD and ex-situ angular dispersive X-ray diffraction on a Philips PW1729 diffractometer in reflection mode at 40 kV and 30 mA, using Cu Kα radiation.

Results

ZPM-I Synthesis. The zinc phosphate monomer was synthesized at room temperature from a gel with the composition $ZnSO_4 \cdot 7H_2O$:$40H_2O$:$[C_6N_2H_{18}][HPO_4] \cdot 2H_2O$. No Bragg reflections were present during the first 70 min of the reaction, at which point three peaks were observed to grow out of the background in the bottom detector. The energies and indices of these peaks were 50.84 (0 1 0), 54.39 [(1 0 0) and (1 0 1)], and 58.63 keV (1 1 1). The limitations in resolution were apparent as the (1 0 0) (7.391 Å) and (1 0 1) (7.258 Å) reflections could not be resolved and appeared as a single peak. A convolution of these two peaks is observed in each reaction. The intensities of the three peaks increased for approximately 40 min, at which point no further increases in intensity were observed. A three-dimensional stack plot of the crystallization of ZPM-I is shown in Figure 3.

ZnPO-TMED-I. Powdered ZPM-I was placed in a 100-fold excess of deionized water and allowed to react at 100 °C. Characteristic ZPM-I reflections were observed in the bottom detector in the first scan, with peaks observed at 50.78 (7.76 Å), 54.37 (7.25 Å), and 58.44 keV (6.73 Å), which correspond to the (0 1 0), (1 0 0) + (1 0 1), and (1 1 1) reflections. The intensities of these reflections decreased to a point at which they were not visible above the background noise after 5 min. A fourth peak was first observed after 2 min of reaction in the bottom detector at 44.49 keV (8.87 Å). The intensity of this peak, which corresponds to the (1 0 0) reflection of ZnPO-TMED-I, increased over the next 10 min, at which point its intensity remained constant during the remainder of the experiment. A three-dimensional stack plot of the transformation of ZPM-I to ZnPO-TMED-I is shown in Figure 4.

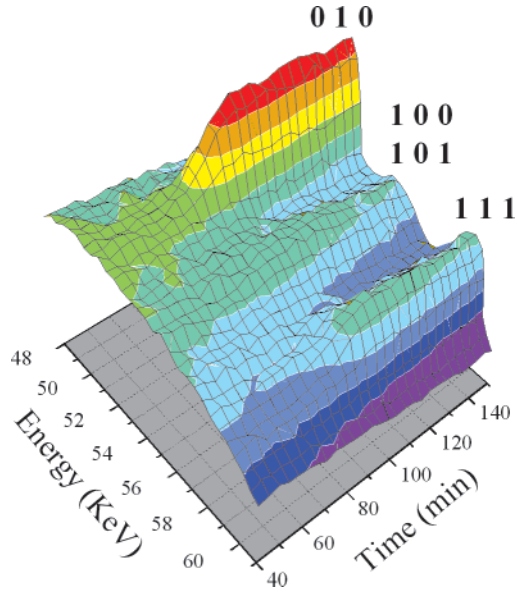

Figure 3. Three-dimensional stack plot of diffraction data collected during the crystallization of ZPM-I at room temperature. Reflection indexes are shown.

ZnPO-PIP-I. An autoclave containing a reaction gel with the composition ZPM-I:piperazine:$250H_2O$ was placed in the heating block, which had been preheated to 60 °C. Three peaks were observed in the first scan, at 50.92, 54.42, and 58.58 keV, which correspond to the (0 1 0), (1 0 0) + (1 0 1), and (1 1 1) reflections at 7.75, 7.25, and 6.74 Å, respectively. The intensities of these ZPM-I peaks decrease quickly and are no longer observed after 7 min. In the seventh minute of the reaction, another peak was observed in the bottom detector at 50.87 keV. This is the (0 1 −1) reflection from ZnPO-PIP-I. The intensity of this peak increases over the next 15 min at which point its intensity remains constant for the rest of the experiment. A three-dimensional stack plot of the transformation of ZPM-I to ZnPO-PIP-I is shown in Figure 5.

ZnPO-IMID-I. Three peaks of low intensity were observed in the first scan of the reaction of a gel containing ZPM-I:2 imidazole:$350H_2O$ at 50 °C. These peaks, present at 50.80, 54.38, and 58.77 keV and from ZPM-I, are not observable after approximately 3 min. No Bragg reflections are observed during the first 30 min of the reaction. At this point, two peaks are observed in the bottom detector at 45.95 and 56.46 keV, the (0

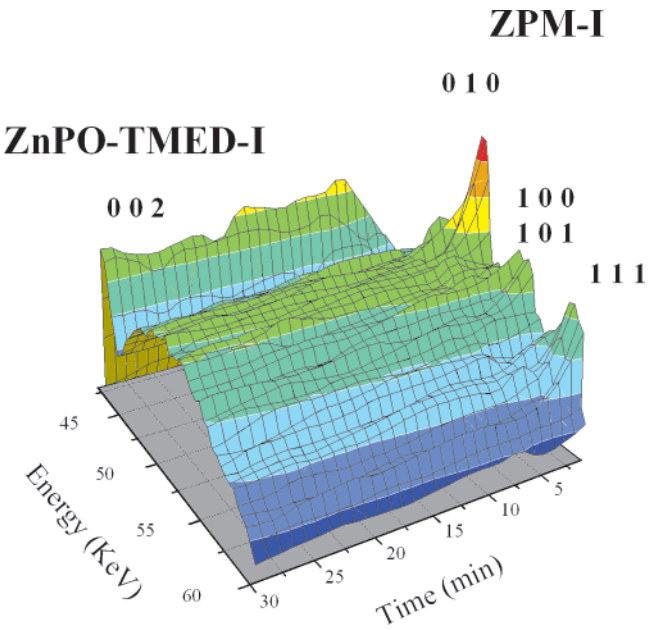

Figure 4. Three-dimensional stack plot of diffraction data collected during the transformation of ZPM-I to ZnPO-TMED-I at 100 °C. Reflection indexes are shown.

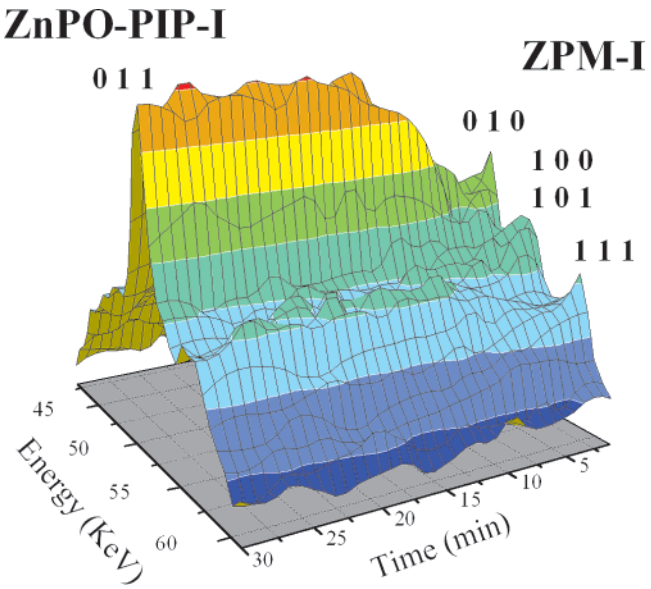

Figure 5. Three-dimensional stack plot of diffraction data collected during the transformation of ZPM-I to ZnPO-PIP-I at 60 °C. Reflection indexes are shown.

0 −2) (8.59 Å) and (0 1 −1) (6.99 Å) reflections of ZnPO-IMID-I. The intensities of these peaks increase over the next 60 min. A three-dimensional stack plot of the transformation of ZPM-I to ZnPO-IMID-I is shown in Figure 6.

The areas of Bragg reflections are integrated using an automated Gaussian fitting routine.[40] These values are converted to extent of reaction (α), scaled from zero to one, using the relationship $\alpha(t) = I_{hkl}(t)/I_{hkl}(\max)$, where $I_{hkl}(t)$ is the area of a given peak at time t, and $I_{hkl}(\max)$ is the maximum area of this peak. The integration of the (0 1 0) ZPM-I reflection is shown in Figure 7a, and the (0 1 0) and (0 0 2) reflections from ZPM-I and ZnPO-TMED-I, respectively, are shown in Figure 8a. Peaks observed in the middle detector were integrated for the conversion of ZPM-I to ZnPO-PIP-I because of overlap between the

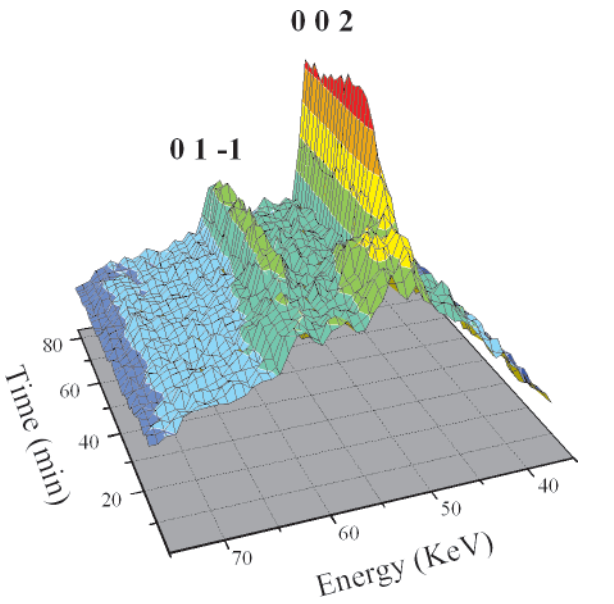

Figure 6. Three-dimensional stack plot of diffraction data collected during the transformation of ZPM-I to ZnPO-IMID-I at 50 °C. Reflection indexes are shown.

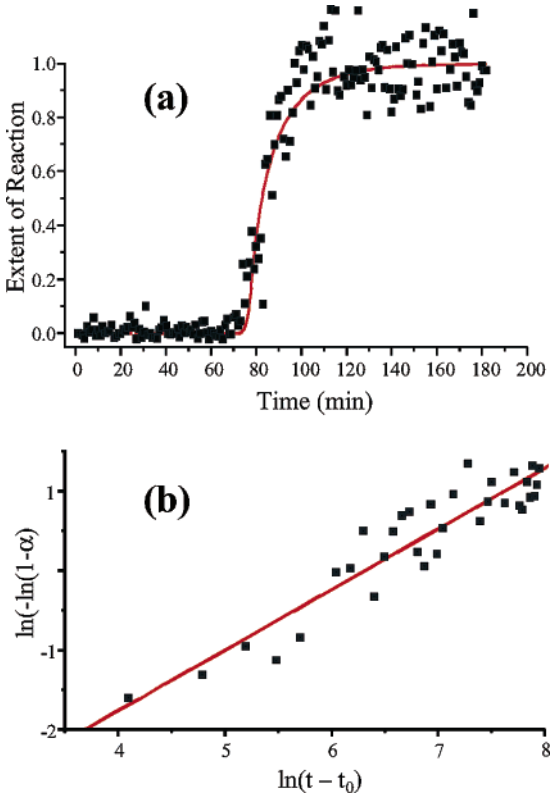

Figure 7. (a) Crystallization curve for ZPM-I. Black squares represent experimental Bragg reflection integration values of the (0 1 0) reflection. The red line corresponds to a fit of the Avrami−Erofe'ev expression using parameters determined using a Sharp−Hancock plot. (b) Sharp−Hancock plot for the formation of ZPM-I at room temperature.

(0 1 0) and (0 1 1) reflections, respectively. The peak integrations shown in Figure 9a are from the (1 3 1) (3.71 Å, 39.69 keV) and (3 2 2) (2.74 Å, 54.25 keV) reflections from ZPM-I and ZnPO-PIP-I. The results of the integration of the (0 0 2) ZnPO-IMID-I reflection are shown in Figure 10a. Plots of

(40) Clark, S. M. *J. Appl. Crystallogr.* **1995**, *28*, 646.

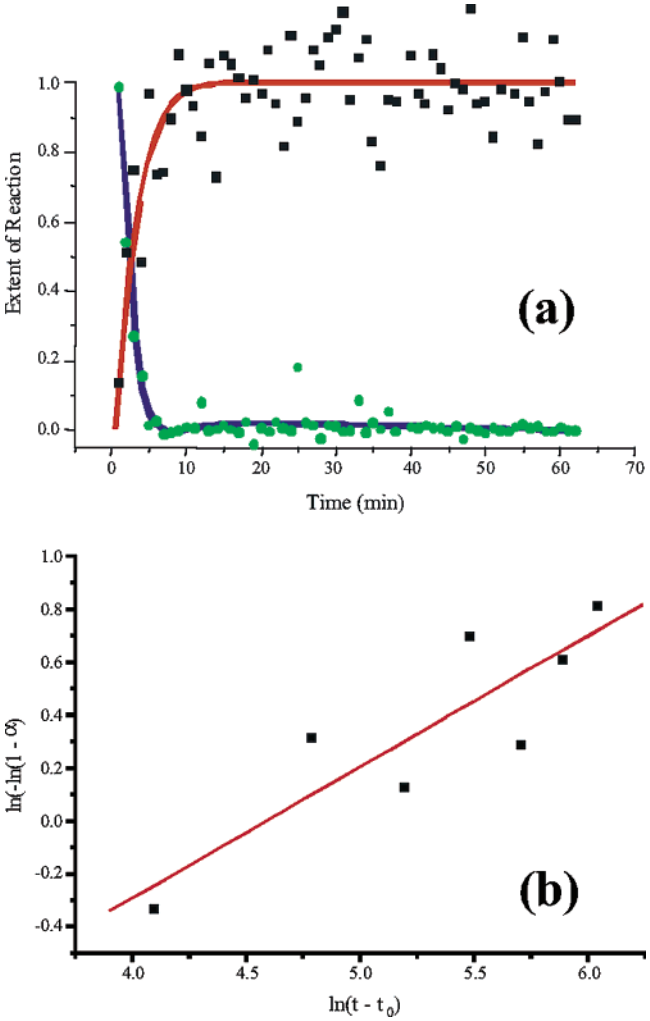

Figure 8. (a) Crystallization curves for ZPM-I (green circles) and ZnPO-TMED-I (black squares) derived from the (0 1 0) and (0 0 2) reflections, respectively. The red line corresponds to a fit of the Avrami−Erofe'ev expression using parameters determined using a Sharp−Hancock plot, and the blue line is present to guide the eye. (b) Sharp−Hancock plot for the formation of ZnPO-TMED-I at 100 °C.

the extent of reaction versus time for each experiment are shown in Figures 7−10.

The Avrami−Erofe'ev expression[41] is widely used to model phase transitions and crystal growth in solid-state chemistry. It relates the extent of reaction, α, to any time *t* using the relationship:

$$\alpha = 1 - \exp[-(k(t - t_0))^n] \qquad (1)$$

where t_0 is the induction time, *k* is the rate constant, and *n* is the Avrami exponent. Mechanistic information can be deduced from the value of the Avrami exponent, *n*. The interpretation of *n* is based upon the work of Hulbert, who analyzed a series of possible ideal reactions and elucidated the value of *n* for each reaction.[42] This expression is found to be most applicable in the range $0.15 < \alpha < 0.8$. The exponent *n*, although sensitive to the nature of the data analysis, can in favorable instances be used to deduce information about the rate of nucleation and

(41) Avrami, M. *J. Chem. Phys.* **1939**, *7*, 1103. Avrami, M. *J. Chem. Phys.* **1940**, *8*, 212. Avrami, M. *J. Chem. Phys.* **1941**, *9*, 177. Erofe'ev, B. V. *C. R. Dokl. Acad. Sci. URSS* **1946**, *52*, 511.
(42) Hulbert, S. F. *J. Br. Ceram. Soc.* **1969**, *6*, 11.

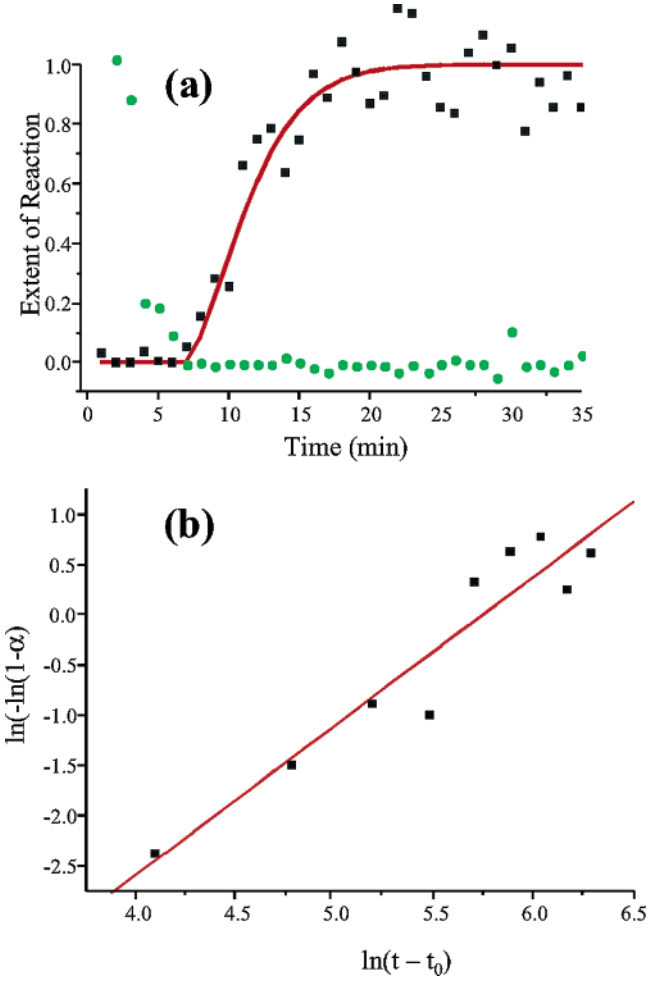

Figure 9. (a) Crystallization curves for ZPM-I (green circles) and ZnPO-PIP-I (black squares) derived from the (1 3 1) and (3 2 2) reflections, respectively. The red line corresponds to a fit of the Avrami−Erofe'ev expression using parameters determined using a Sharp−Hancock plot. (b) Sharp−Hancock plot for the formation of ZnPO-PIP-I at 60 °C.

the mechanism of nuclei growth. The value of *n* is most easily obtained using a Sharp−Hancock plot,[43] which is a plot of $\ln\{-\ln(1 - \alpha)\}$ against ln(time) that gives a straight line of gradient *n* and intercept $n \ln k$. The graphs produced are linear over the whole extent of data, and the gradient and intercept of lines fitted by linear regression allow kinetic parameters to be extracted. Parameters obtained by analysis of data collected during the preparation of ZPM-I, and its transformation to ZnPO-TMED-I, ZnPO-PIP-I, and ZnPO-IMID-I, are listed in Table 2. Sharp−Hancock plots for each reaction and a fit of the Avrami−Erofe'ev expression using parameters obtained from the Sharp−Hancock plots are shown in Figures 7b−10b.

Discussion

The Avrami exponents calculated from Sharp−Hancock plots contain important mechanistic information about each reaction studied. The values obtained from the Sharp−Hancock plots were checked by plotting the experimental data over an extent of reaction curve calculated from the Avrami−Erofe'ev expression, using these values. See Figures 7a−10a. A value of $n = 0.76$ was calculated for the crystallization of ZPM-I, which corresponds to a diffusion-controlled process. That is, the rate

(43) Hancock, J. D.; Sharp, J. H. *J. Am. Ceram. Soc.* **1972**, *55*, 74.

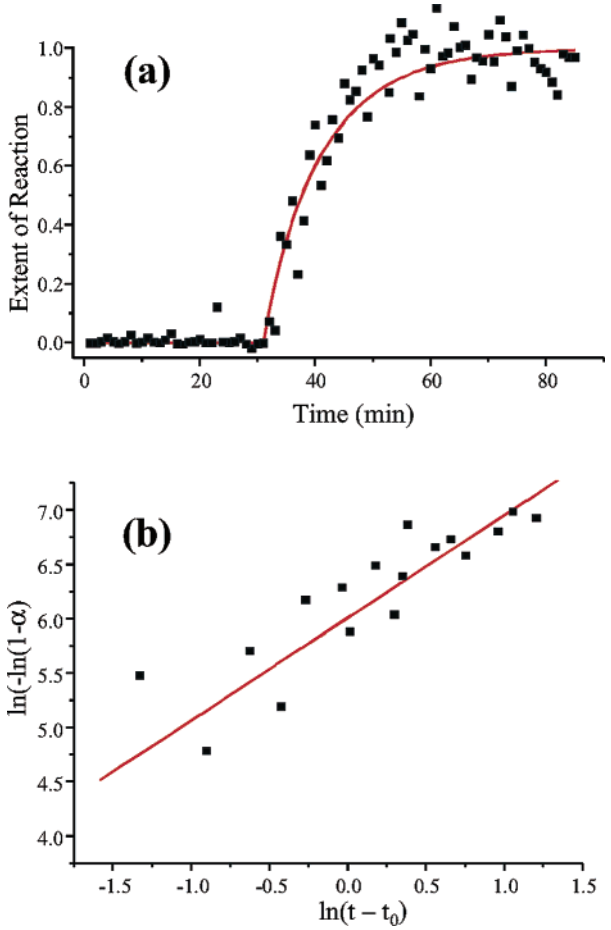

Figure 10. (a) Crystallization curve for ZnPO-IMID-I derived from the (0 0 2) reflection. The red line corresponds to a fit of the Avrami−Erofe'ev expression using parameters determined using a Sharp−Hancock plot. (b) Sharp−Hancock plot for the formation of ZnPO-IMID-I at 50 °C.

Table 2. Results of Sharp−Hancock Analysis of ZPM-I Synthesis and Transformations[a]

				Avrami model	
compound	temp (°C)	t_0 (s)	*h k l*	*n*	*k* (s^{-1})
ZPM-I	25	4620	0 1 0	0.76	1.81×10^{-3}
ZnPO-TMED-I	100	0	0 0 2	1.16	4.70×10^{-3}
ZnPO-PIP-I	60	240	3 2 2	1.48	3.17×10^{-3}
ZnPO-IMID-I	50	1740	0 0 2	0.94	1.69×10^{-3}

[a] Kinetic curves were derived from the Bragg reflections listed. The induction time, t_0, was determined by inspection and is the time it took for Bragg reflections to appear above background noise. *n* is the Avrami exponent, and *k* is the rate constant for the crystallization.

of the reaction only depends on the rate of diffusion of the reactive species through the solution to the site of crystallization. The relative rate of the formation of nucleation sites, the rate of dissolution of starting materials, or the rate of crystal growth on the surface of each crystallite are each significantly fast with respect to the rate of diffusion.

The transformation of ZPM-I to ZnPO-TMED-I has a calculated Avrami exponent of 1.16, from which a change in reaction mechanism can be inferred with respect to the crystallization of ZPM-I. It is understood that as *n* becomes larger the rate of the formation of nucleation sites becomes increasingly important in determining the overall rate of crystallization.

The transformation of ZPM-I to ZnPO-PIP-I and ZnPO-IMID-I also exhibits Avrami exponents that are significantly

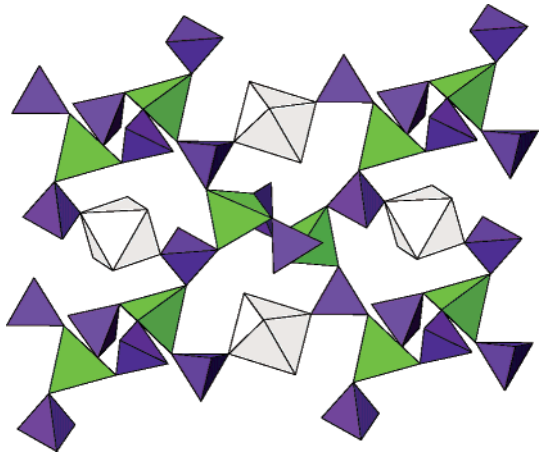

Figure 11. Representation of the inorganic layer in ZnPO-TMED-I. The $[Zn_2(HPO_4)_6]$ dimers are shown as green and purple tetrahedra for $[ZnO_4]$ and $[HPO_4]$, respectively. The $[ZnO_2(H_2O)_4]$ octahedra are shown in gray.

higher with respect to the crystallization of ZPM-I. Two things can be inferred for this shift and the nature of the extent of reaction curves that correspond to both the ZPM-I starting material and the ZnPO-PIP-I and ZnPO-IMID-I products. First, the formation of nucleation sites is more important in the determination of the overall rate of crystallization than dissolution of reactive species, the diffusion of these species to the site of crystallization, or the rate of growth on the surface of each crystallite. Second, the nucleation-controlled formation of ZnPO-PIP-I and ZnPO-IMID-I occurs via a dissolution−reprecipitation process. That is, both the ZPM-I and the amines dissolve before reaction, and no solid-state transformation is observed. This can be elucidated from the extent of reaction curves. See Figures 9a and 10a. In the formation of ZnPO-PIP-I, essentially all of the ZPM-I has been dissolved, as observed by the near absence of characteristic Bragg reflections before any intensity is present in Bragg reflections that correspond to ZnPO-PIP-I. In the formation of ZnPO-IMID-I (Figure 10a), very little intensity from ZPM-I reflections was observed even in the first few minutes of reaction. By the time ZnPO-IMID-I reflections were first observed (approximately 30 min), the crystalline ZPM-I had long since dissolved. Also, a dramatic difference in the Zn^{2+} coordination is present between ZPM-I and ZnPO-IMID-I. Each Zn dication resides at the center of a ZnO_4 tetrahedron in ZPM-I, while in ZnPO-IMID-I direct bonding between the imidazole rings and each Zn^{2+} is observed.

Analysis of the data collected during the conversion of ZPM-I to ZnPO-TMED-I at 100 °C in water does not suggest a dissolution−reprecipitation mechanism. Instead, a direct topochemical transformation appears to occur. This assignment is consistent with both the observed extent of reaction curves and the presence of ZPM-I dimers in the ZnPO-TMED-I inorganic layers. If a direct topochemical transformation is observed, the extent of reaction curves should cross at 0.5 because crystalline material is neither gained nor lost during the reaction. At any time *t*, the total amount of the crystalline starting material plus product should remain constant. The extent of reaction curves, as shown in Figure 8a, cross at approximately 0.5, as expected for a direct structural transformation. There are minimal structural differences between ZPM-I and ZnPO-TMED-I. In fact, the structural motif of the $[Zn_2(HPO_4)_2(H_2PO_4)_4]$ is easily observed in the inorganic layer of ZnPO-

TMED-I, see Figure 11. One-third of the Zn^{2+} exhibits an altered coordination environment after the transformation. Four water molecules displace bound phosphate tetrahedra, resulting in $[ZnO_2(H_2O)_4]$ coordination octahedra. The inclusion of water and overall displacement of phosphate is expected as only two reactants are present, ZPM-I and water.

The transformation of the low-dimensional ZPM-I to compounds containing inorganic components of higher dimensionality has been studied extensively by Rao et al. We were able to use our noninvasive in-situ hydrothermal probe to monitor these reactions and elucidate both kinetic and mechanistic information under real laboratory conditions. The formation of ZPM-I is a diffusion-controlled process, while the formation of ZnPO-TMED-I, ZnPO-PIP-I, and ZnPO-TMED-I are all nucleation controlled. The high solubility of ZPM-I in water, even at room temperature, results in the transformations to ZnPO-PIP-I and ZnPO-IMID-I exhibiting dissolution−reprecipitation mechanisms. The reaction of ZPM-I in water at 100 °C appears to be a direct topochemical transformation to ZnPO-TMED-I and, to the best of our knowledge, the first direct observation of a topochemical transformation.

Acknowledgment. We thank the EPSRC for support.

JA049860W